A Comparison of Near-Surface Buoyancy and Baroclinity across Three VORTEX2 Supercell Intercepts

CHRISTOPHER C. WEISS

Department of Geosciences, Texas Tech University, Lubbock, Texas

DAVID C. DOWELL

NOAA/Earth System Research Laboratory, Boulder, Colorado

JOHN L. SCHROEDER, PATRICK S. SKINNER,* AND ANTHONY E. REINHART

Department of Geosciences, Texas Tech University, Lubbock, Texas

PAUL M. MARKOWSKI AND YVETTE P. RICHARDSON

Department of Meteorology, The Pennsylvania State University, University Park, Pennsylvania

(Manuscript received 24 September 2014, in final form 6 February 2015)

ABSTRACT

Observations obtained during the second Verification of the Origin of Rotation in Tornadoes Experiment (VORTEX2) are analyzed for three supercell intercepts. These intercepts used a fleet of deployable "StickNet" probes, complemented by mobile radars and a mobile mesonet, to map state quantities over the expanse of target storms.

Two of the deployments occurred for different stages of a supercell storm near and east of Dumas, Texas, on 18 May 2010. A comparison of the thermodynamic and kinematic characteristics of the storm provides a possible explanation for why one phase was weakly tornadic and the other nontornadic. The weakly tornadic phase features a stronger horizontal virtual temperature gradient antiparallel to the forward-flank reflectivity gradient and perpendicular to the near-surface flow direction, suggesting that air parcels could acquire more significant baroclinic vorticity as they approach the low-level mesocyclone.

The strongly tornadic 10 May 2010 case near Seminole, Oklahoma, features comparatively small virtual and equivalent potential temperature deficits, suggesting the strength of baroclinic zones may be less useful than the buoyancy near the mesocyclone for assessing tornado potential. The distribution of positive pressure perturbations and backed ground-relative winds within the forward flank are consistent with the notion of a "starburst" pattern of diverging winds associated with the forward-flank downdraft.

Narrow (~1 km wide) zones of intense baroclinic vorticity generation of $O(\sim 10^{-4})\,\mathrm{s}^{-2}$ are shown to exist within precipitation on the forward and left sides of the mesocyclone in the Dumas intercepts, not dissimilar from such zones identified in recent high-resolution numerical studies.

* Current affiliation: National Severe Storms Laboratory, Norman, Oklahoma.

Corresponding author address: Christopher C. Weiss, Department of Geosciences, Texas Tech University, Box 41053, Lubbock, TX 79409.
E-mail: chris.weiss@ttu.edu

1. Introduction

The manner in which low-level mesocyclones acquire their vorticity has been a subject of considerable focus in prior studies. A growing body of evidence (e.g., Markowski et al. 2012a,b; Skinner et al. 2014) supports the notion that influences on vertical vorticity near the surface and at "middle" (e.g., 3–5 km AGL) levels of the troposphere—particularly early in the life of the storm before significant low-level vorticity is ingested and

advected upward—are rather exclusive of each other, the latter primarily a result of tilting and stretching of environmental (predominantly horizontal) vorticity by the updraft (Brandes 1978; Rotunno 1981; Davies-Jones 1984). However, the lateral proximity of these areas of vertical vorticity appears to have some bearing on the amplification of rotation near the surface as the vertical acceleration necessary for stretching the low-level vorticity depends partly on the location of the midlevel circulation (e.g., Dowell and Bluestein 2002a,b; Marquis et al. 2012; Markowski and Richardson 2014; Skinner et al. 2014).

The baroclinic generation of (predominantly horizontal) vorticity by horizontal buoyancy gradients associated with the precipitation region of supercells has received considerable attention. The numerical simulations of Klemp and Rotunno (1983) and Rotunno and Klemp (1985) were the first to quantify baroclinically generated horizontal vorticity, reaching magnitudes of $10^{-2}\,\mathrm{s}^{-1}$ over a path of 5 km, for air parcels traveling through lateral gradients of air density resulting from latent chilling and hydrometeor loading within the precipitation region. A number of subsequent modeling studies have further elucidated the role of baroclinic zones in modulating the low-level vertical vorticity, (e.g., Wicker and Wilhelmson 1995; Adlerman et al. 1999; Beck and Weiss 2013). Further, material circuits integrated backward in time from observed and simulated low-level mesocyclones (e.g., Rotunno and Klemp 1985; Davies-Jones and Brooks 1993; Markowski et al. 2012b; Markowski and Richardson 2014) have been shown to acquire circulation solenoidally as portions of the circuits pass through the southern edge of the forward-flank precipitation region.

Significant baroclinic zones were noted by Beck and Weiss (2013) within the body of simulated forward- and left-flank precipitation.[1] Initially, multiple zones of baroclinity and convergence were formed from periodic bursts of outflow within the forward flank of their simulations; these zones then consolidated into a single area with a horizontal baroclinic vorticity tendency of $O(\sim 10^{-4})\,\mathrm{s}^{-2}$. This zone was well to the northwest of, and oriented at a considerable angle to, the baroclinic boundary along the right edge of the forward-flank precipitation. As Dahl et al. (2014) similarly demonstrated through simulation,

numerous "rivers" of vertical vorticity can arise as descending parcels experience horizontal baroclinic vorticity generation and subsequent tilting along their path. There are very few observations to verify the presence of these zones.

Previous attempts to observe the thermodynamic characteristics of the air feeding the near-surface mesocyclone have relied primarily on mobile mesonet instrumentation (Straka et al. 1996; Waugh and Fredrickson 2010). The consensus from these studies is that strongly tornadic cases feature more limited density excesses within near-surface outflow near the location of the low-level mesocyclone (e.g., Markowski et al. 2002; Grzych et al. 2007; Hirth et al. 2008; Skinner et al. 2011; Lee et al. 2011, 2012; Markowski et al. 2012a,b; Kosiba et al. 2013) and farther into the forward-flank precipitation (Shabbott and Markowski 2006) where critical baroclinic vorticity is identified in numerical simulations. Skinner et al. (2011) documented that the equivalent potential temperature within the forward-flank baroclinic zone of the 2007 Perryton, Texas, storm was actually *higher* than in the environment, and thus there was a favorable juxtaposition of solenoidal horizontal vorticity generation and anomalously high potential buoyancy.

This study presents a comparison of three surface analyses during the second Verification of the Origin of Rotation in Tornadoes Experiment (VORTEX2; Wurman et al. 2012) in 2009–10. Most of the data presented were collected by an array of Texas Tech University "StickNet" in situ probes, which were tasked with the storm-scale mapping of the thermodynamic and kinematic state within target VORTEX2 storms. As such, it is possible to assess the distribution of buoyancy and detect regions of baroclinity over a broad swath.

Two of the three StickNet deployments selected for study are from the same VORTEX2 case (18 May 2010, near and east of Dumas, Texas). Since the proclivity for (weak) tornado production varied between the two deployments, though the inflow environment was quite similar, the analyses (approximately 1 h apart) allow for a compelling comparison. The third case, from 10 May 2010 near Seminole, Oklahoma, provides observations of a strongly tornadic enhanced Fujita scale (EF3) storm for further comparison. Section 2 provides a background of the StickNet instrumentation used in this study, while section 3 describes the analysis methods used. An overview of the cases is presented in section 4, and sections 5 and 6 include results and a discussion, respectively.

---

[1] The designation of the "forward" and "rear" flank follows a similar convention to that of Shabbott and Markowski (2006), either side of a line placed orthogonal to the major axis of the radar echo and through the center of the mesocyclone at radar level. For regions near this dividing line, to the left of the mesocyclone looking downshear, we add the designation "left flank" in line with that discussed by Beck and Weiss (2013).

2. StickNet

The StickNet platforms were first conceived as part of a multidisciplinary course project at Texas Tech University
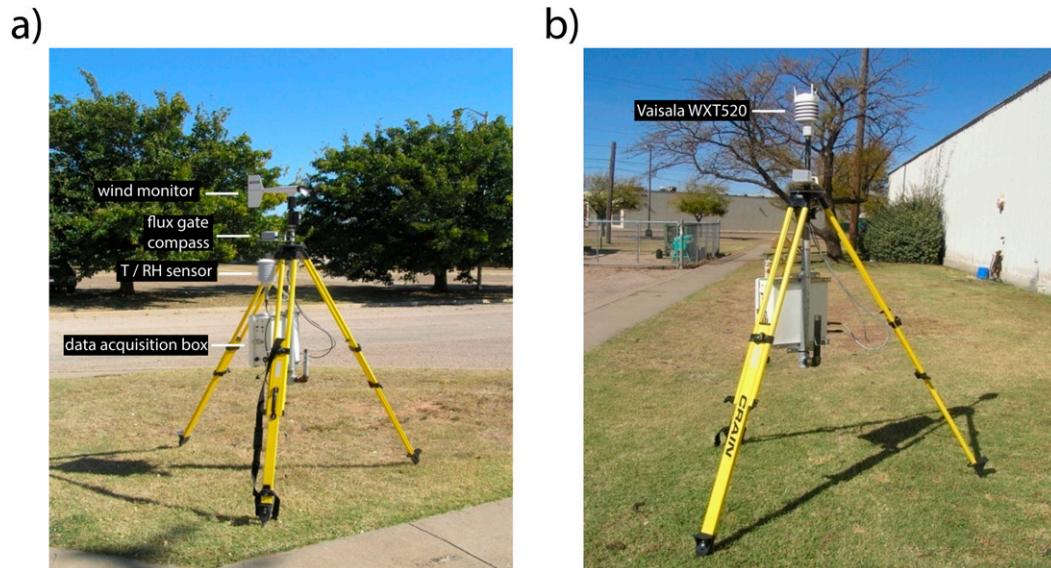
FIG. 1. Photographs of StickNet (a) type-A and (b) type-B probes. Specific attributes of the design are highlighted.

in 2005. Faculty and students worked together to design a ruggedized, rapidly deployable (~2 min) in situ probe to be used in the sampling of severe thunderstorms. Details of StickNet construction and associated educational objectives are given by Schroeder and Weiss (2008).

A total of 24 StickNet probes were available for the VORTEX2 project. At the beginning of the VORTEX2 field phase in 2009, 14 of these probes were classified as type "A" (Fig. 1a), with separate instrument components dedicated to the sampling of individual atmospheric state variables (temperature, humidity, pressure, and wind). Ten probes, referred to as type "B" (Fig. 1b), utilized the Vaisala WXT510 (upgraded to WXT520 for 2010) all-in-one sensor, which collects all state variables within the same instrument housing. Rainfall and hailfall are additionally sensed acoustically in the type-B architecture. Features common to both probe types include the following: a flux gate compass, needed for adjusting wind measurements to earth-relative coordinates; a GPS receiver; an internal lithium battery (18-h capacity); a voltage regulator; and ports for Ethernet output and external power. Probes were delivered to the field with four deployment vehicles and two trailers, each capable of data transfer and recharging while in transit. For type-A probes, data sampling is adjustable between 1 and 10 Hz, while the sampling for type-B probes is fixed at 1 Hz.

The total number of individual StickNet probe deployments was 650 during the two field seasons of the VORTEX2 project. A list of notable deployments is included in Table 1. Though many deviations were necessary over the span of field deployments, the default deployment pattern was two equal arrays oriented normal to the storm motion. A coarse array of probes (approximately 20–30 km wide, with 4–6-km spacing) was placed in an attempt to capture the storm-scale thermodynamic footprint, with a nested fine array (approximate 5 km wide, with 1-km spacing) to sample regions near the low-level mesocyclone where sharper gradients were expected to exist [see Fig. 7 in Wurman et al. (2012)].

As with any in situ platform, the response time of StickNet temperature and humidity sensors will necessarily displace the position of extrema of thermodynamic state quantities and serve to weaken gradients thereof. Following the investigation by Skinner et al. (2010), calculated time constants are multiplied into the observed storm motion for each case to yield distance constants for this study (Table 2), representing the distance over which an instrument will achieve a $1 - e^{-1}$ (63%) response to a step change.

3. Analysis method

All StickNet data were first quality controlled to remove clearly erroneous observations and dropouts, with subsequent subjective inspection for questionable observations as described by Skinner et al. (2011). Portions of the observation record were removed in isolated cases owing to known instrumentation issues, some owing to storm damage, identified after data collection was completed. (These instrumentation issues are documented in the StickNet datasets available on the VORTEX2 field catalog.) A 5-s moving average was then applied to these data.

Biases were removed from quality-controlled StickNet data according to the results of periodic intercomparison

TABLE 1. A list of notable StickNet deployments from VORTEX2.

Date	Event description	Deployments
15 May 2009	Squall line near Jet, OK	2
23 May 2009	Multicell storm east of Ogallala, NE	1
4 Jun 2009	Supercell near Cheyenne, WY	1
5 Jun 2009	Tornadic supercell near Lagrange, WY	2
6 Jun 2009	Supercell near Thedford, NE	1
7 Jun 2009	Supercell near Oregon, MO	2
9 Jun 2009	Supercell near Greensburg, KS	2
11 Jun 2009	Merging supercells near La Junta, CO	2
13 Jun 2009	Supercells near Panhandle and White Deer, TX	2
10 May 2010	Tornadic supercell near Seminole, OK	1
12 May 2010	Supercell near Sayre, OK	2
14 May 2010	Tornadic supercell, bow echo near Odessa, TX	1
15 May 2010	Supercell near Artesia, NM	2
17 May 2010	Supercell near Artesia, NM	1
18 May 2010	Supercell near Dumas, TX	2
19 May 2010	Supercell near Cimarron City, OK	2
23 May 2010	Supercell near Leoti, KS	1
24 May 2010	Supercells near Sutherland and Gothenberg, NE	2
25 May 2010	Tornadic supercell near Tribune, KS	2
26 May 2010	Supercell near Wiggins, CO	1
2 Jun 2010	Supercell near Benkelman, NE	2
3 Jun 2010	Supercell near Niobrara, NE	1
6 Jun 2010	Merging supercells near Ogallala, NE	1
7 Jun 2010	Tornadic supercells near Mitchell and Bridgeport, NE	2
9 Jun 2010	Supercells near Stegall and Scottsbluff, NE	2
10 Jun 2010	Tornadic supercell near Last Chance, CO	1
11 Jun 2010	Supercell near Limon, CO	2
12 Jun 2010	Elevated supercells near Gruver, TX	1
13 Jun 2010	Tornadic supercell near Booker, TX	3
14 Jun 2010	Multicell storm near Post, TX	1

mesocyclone and a persistent reflectivity maximum [determined from Doppler on Wheels (DOW6; Wurman et al. 1997) and Shared Mobile Atmospheric Research and Teaching Radar (SMART-R1; Biggerstaff et al. 2005) data] immediately northwest of the low-level mesocyclone yielded an average storm motion of $u = 9.25$, $v = 0.35 \, \mathrm{m \, s^{-1}}$ over the period 2300–0100 UTC. A similar reflectivity feature and radar-level mesocyclone/tornado motion yield a storm-motion estimate of $u = 23.95$, $v = -0.15 \, \mathrm{m \, s^{-1}}$ for the Seminole case, calculated for the period 2250–2350 UTC. These data were then objectively analyzed to a 2D (horizontal) 500-m grid using an isotropic two-pass Barnes filter (Barnes 1964), with the convergence parameter $\gamma = 0.1$ and shape parameter $\kappa = (1.33\Delta d)^2$, where Δd represents the mean along-deployment line (nearly north–south in the cases presented here) station spacing, equal to 4.20, 4.09, and 5.92 km for the first Dumas deployment (D1WT), second Dumas deployment (D2NT), and Seminole deployment (ST), respectively.

Mobile radar and WSR-88D data, which provide storm-scale context for the StickNet observations, were subjected to a separate Barnes's filter [similar to Majcen et al. (2008)], with $\gamma = 0.3$ and $\kappa = 1.33\mu$ (Pauley and Wu 1990); here, μ represents the coarsest spatial resolution of radar data represented by the product $R_{\max}\theta$ (Trapp and Doswell 2000), where $R_{\max}$ is the maximum range of analyzed data from the radar and θ is the angular beamwidth. Data from the Amarillo, Texas (KAMA), WSR-88D, DOW6, SMART-R1, and KOUN WSR-88D prototype (in Norman, Oklahoma) were objectively analyzed. Reflectivity data from DOW6 are uncalibrated; a correction of $+20 \, \mathrm{dB}Z$ is crudely estimated from comparisons to WSR-88D in regions of negligible X-band attenuation.

The origin (0, 0) of all StickNet and radar analyses represents the position at which the low-level maximum in azimuthal shear of radar radial velocity (from 1- to 10-km width) intersects a straight line drawn through the entire StickNet deployment (the longitude of this position is hereafter referred to as X_{crossing}). Composite profiles are produced by averaging radar and atmospheric state fields in this same low-level mesocyclone-relative coordinate system. Radar data are chosen for the time period nearest the time of this crossing, with no more than 180 s of disparity in time.

Endemic to the use of time-to-space conversion is the assumption of the Taylor hypothesis (Taylor 1938) over the period of analysis. As the time-to-space conversion is centered on individual instruments at a reference time, the assumption is increasingly restrictive with absolute (converted) distance from the instrument. Given the nearly north–south deployments in our cases, errors

tests conducted throughout the VORTEX2 field phase. During these tests, StickNet probes were deployed in close proximity to one another, spaced approximately 3 m apart, and collected contemporaneous data for over 30 min. Probes were corrected for their difference from the full-fleet mean. For the 18 May and 10 May 2010 cases near Dumas and Seminole, respectively, an intercomparison test performed the day prior to each event was utilized.

Time-to-space conversion was performed on the StickNet data using a constant estimated storm motion. For the Dumas case, the motion of both the low-level

TABLE 2. Distance constants calculated for StickNet instrumentation used in this study.

Ground-relative wind speed (aspiration)	18 May 2010 (motion 9.28 m s^{-1})		10 May 2010 (motion 23.95 m s^{-1})	
	10 kt	20 kt	10 kt	20 kt
"xxA" probe T	0.72 km	0.63 km	1.87 km	1.63 km
"xxA" probe RH	0.95 km	0.74 km	2.47 km	1.92 km
"xxB" probe T	1.90 km	1.65 km	4.91 km	4.26 km
"xxB" probe RH	1.95 km	1.79 km	5.03 km	4.62 km

increase in our analyses according to the distance from $X_{crossing}$. The maximum periods used in this study [25 (30) min for the Dumas (Seminole)] exceed periods used in prior studies [e.g., 5 min in Markowski et al. (2002) and Skinner et al. (2011); 10 min in Shabbott and Markowski (2006) and Hirth et al. (2008)]. However, we contend these periods are justified as 1) many conclusions in this study are relevant to the storm scale and errors in applying the Taylor hypothesis do not affect the identification of storm-scale regions (e.g., forward, rear flank) over the time period used, 2) conclusions that are related to smaller-scale variations (e.g., the position of the forward-flank reflectivity gradient) are in close enough proximity to $X_{crossing}$ such that the stationarity assumption is adequate and in line with previous studies, and 3) inflections in StickNet wind measurements across the entire domain agree reasonably with those indicated from radar data obtained near the reference time (e.g., regions of diffluence near $x = -8$ and the wind shift within the forward flank near $x = 8$, $y = 12$, presented later in Fig. 3d), notwithstanding the difference in altitude between these radar and in situ measurements, confirming that the broader time-to-space conversion is reasonably placed relative to the regions and boundaries discussed.

Pseudoequivalent potential temperature is calculated as in Bolton (1980). Virtual potential temperature is computed according to the following standard formulation:

$$\theta_v = \theta(1 + 0.61q_v), \quad (1)$$

where θ denotes potential temperature and q_v represents the water vapor mixing ratio. The calculation of density potential temperature, which factors in the contribution of liquid condensate to air density, was not possible for the Dumas case since only the two Doppler on Wheels radars, which had an uncalibrated reflectivity factor, were positioned close enough to the first StickNet deployment line for sufficient spatial resolution.[2] Similarly, no mobile radar data were available for the Seminole case.

A base state is chosen that best represents the environment of each storm. For the analyses presented herein, we choose to use a representative observation within the inflow environment known to be outside obvious convective processes (e.g., outflow, anvil shadow) (e.g., Skinner et al. 2011) and at the proper distance ahead of the storm such that these parcels were near the updraft at the center of each analysis period. These observations are detailed in Table 3. StickNet observations were prioritized, though surrounding observations from the mobile GPS Advanced Upper Air Sounding (GAUS) systems were considered as well [e.g., on 18 May 2010, the lowest-altitude point of the NSSL2 (2256 UTC) and NCAR2 (2258 UTC) soundings was within 0–2 K of the StickNet base-state values for θ_v and θ_e for the first deployment]. In the 10 May 2010 case, StickNet probes were affected by forward-flank precipitation at the time of deployment, requiring the use of an Oklahoma Mesonet observation. The pressure at all observation sites is reduced to mean sea level using a standard hydrostatic relationship, $P_o = Pe^{z/H}$, where P is the station pressure, z is the station altitude (derived from the 30-m resolution digital elevation model available on Google Earth), and H is the standard scale height of 8.65 km. All reported pressure perturbations are those that exist following the reduction to mean sea level.

4. Case overviews

a. 18 May 2010, Dumas, Texas

On 18 May 2010, VORTEX2 intercepted an isolated supercell in the northern Texas Panhandle. Deep convection first formed shortly after 2100 UTC in southwestern Hartley County, Texas. The storm rapidly became severe and, over the following two hours, experienced frequent mergers with ancillary cells that had formed to the south along the dryline. Following one such merger near 2245 UTC, when the updraft was approximately 15 km west of Dumas a period ensued during which the storm generated multiple high-frequency surges within the rear-flank downdraft (Skinner et al. 2014).

---

[2] Even with calibrated reflectivity data, errors accrue in the calculation of θ_ρ owing to the relationship of reflectivity to hydrometeor mass, and the effects of attenuation.

TABLE 3. Surface observations used to define the base state for the three cases.

Case	Time (UTC)	Time (min) prior to center of StickNet analysis	Heading(°)/distance (km) from low-level mesocyclone	Type	θ_v (K)	θ_e (K)
10 May 2010 (ST)	2304	14	115°/26	OK Mesonet [Bowlegs (BOWL) station]	303.18	345.20
18 May 2010 No. 1 (D1WT)	2305	25	103°/16.7	StickNet (probe 23A)	307.68	340.77
18 May 2010 No. 2 (D2NT)	0000 (19 May)	25	128°/14.6	StickNet (probe 01A)	306.28	341.03

A number of weak (EF0) tornadoes were reported with this storm between 2232 and 2345 UTC near and to the west of Dumas (Fig. 2a). The first of two StickNet deployments (hereafter D1WT) began at 2222 UTC approximately 30 km to the north of Dumas with probes deployed approximately north–south, and ended at 2302 UTC approximately 10 km south of Dumas (Fig. 2a). Scheduled deployments were interrupted as probes could not be deployed within the city limits of Dumas. A weak

tornado, observed by DOW6 5 km to the south of Dumas at 2328 UTC, passed through the StickNet array, though no probes were directly impacted.

No tornadoes were reported from 2342 to 0044 (19 May) UTC as the target storm progressed into the open country east of Dumas and through a second StickNet line (hereafter D2NT), deployed between 2306 and 0003 UTC along FM-1060 in eastern Moore County, Texas (Fig. 2b). As the updraft of the target storm
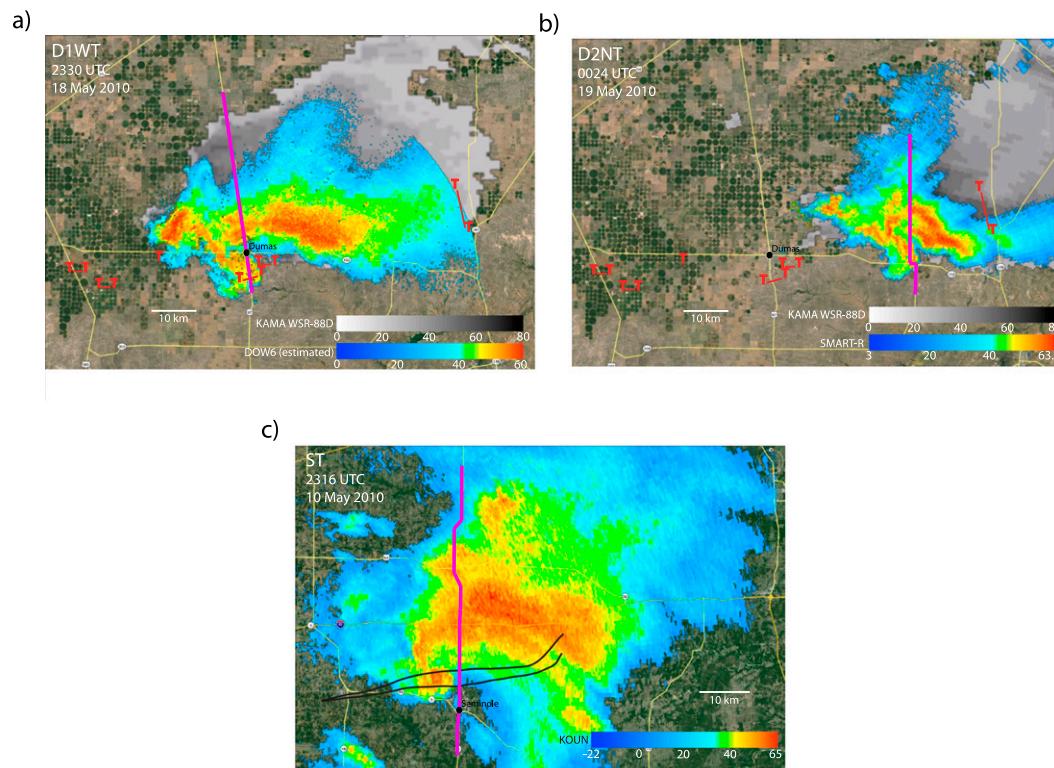

FIG. 2. (a) A map overlaying DOW6 2.0° elevation reflectivity [color shaded, dBZ (estimated), scale at bottom right], valid at 2330 UTC 18 May 2010; NWS KAMA WSR-88D reflectivity (gray shaded, dBZ, scale at bottom right); and the footprint of StickNet probe deployments (purple line). The paths of confirmed tornadoes (red lines bookended with Ts) are derived from the National Climatic Data Center Storm Events Database. (b) As in (a), but mobile radar data (color shaded, dBZ, scale at bottom right) are from the 1.6° elevation SMART-R1 PPI, valid at 0024 UTC (19 May 2010). (c) As in (a), but radar data (color shaded, dBZ, scale at bottom right) are from the 0.5° elevation KOUN PPI scan, valid at 2316 UTC 10 May 2010 and the tornado path (bordered by black curves) is adopted from the damage survey performed by the National Weather Service in Norman, OK (the indicated path terminates at the end of the survey, not at the actual end of the tornado path farther east). The distance scale is indicated.

passed through the probe array at approximately 0025 UTC, low-level (approximately 200 m AGL) maximum vertical vorticity inferred[3] from single-Doppler Naval Postgraduate School Mobile Weather Radar-2005, X-band, Phased-Array (MWR-05XP) measurements at 0024 UTC is $0.03\,s^{-1}$, approximately a full order of magnitude weaker than in the vortex scanned by DOW6 at 2330 UTC near D1WT ($0.21\,s^{-1}$; also at approximately 200 m AGL).[4] Combined with the pattern of tornado reports (Figs. 2a,b), we choose to classify the D1WT deployment as ''weakly tornadic'' and the D2NT as ''nontornadic,'' motivating a direct comparison of the thermodynamic and kinematic environments between the two deployments.

b. 10 May 2010, Seminole, Oklahoma

An outbreak of rapidly moving tornadic supercells occurred across southern Kansas and Oklahoma during the afternoon and evening hours of 10 May 2010 [e.g., as discussed by Palmer et al. (2011)]. The longest path was associated with an EF3 tornado that developed near Tecumseh, Oklahoma, traveled east-northeastward, crossed US 377 north of Seminole and continued past Cromwell, Oklahoma.

StickNet teams were able to deploy 10 probes in a north–south line from approximately 5 km south of Stroud, Oklahoma (first probe drop at 2222 UTC), to 9 km south of Seminole (last probe drop at 2325 UTC), the deployment hereafter referred to as ST (Fig. 2c). The low-level mesocyclone and associated tornado passed through the StickNet array at 2320 UTC. [The maximum StickNet-observed wind speed ($34.3\,m\,s^{-1}$) was recorded by probe 0105A at 2320:03 UTC as the tornado passed south of the platform.] Even though there was limited lead time on this deployment compared to D1WT and D2NT, an adequate sample of the forward flank was obtained for purposes of a comparison with D1WT and D2NT.

---

[3] Vertical vorticity is inferred assuming the azimuthal wind profile of a Rankine vortex, calculated as

$$2/r(\partial V_r/\partial \phi),$$

where V_r is the radial velocity and ϕ is the azimuthal angle. The finite-difference form of this equation is applied over a span of azimuthal width from 1 to 10 km; the maximum is reported here.

[4] For comparison to MWR-05XP radar measurements (1.8° beamwidth), degraded DOW6 measurements (0.93° original beamwidth) were produced by simple averaging of radial velocity data from adjacent azimuths. Though the effective resolution of the degraded DOW6 measurements is similar to that of MWR-05XP, the degraded DOW6 vorticity estimate for D1WT ($0.18\,s^{-1}$) is still an order of magnitude stronger than the MWR-05XP vorticity estimate for D2NT.

5. Results

a. Magnitude and position of minimum θ_v and θ_e perturbations

The time-to-space converted StickNet analysis for the D1WT deployment reveals a significant cold pool (Figs. 3a,b), where minimum perturbations in θ_v (θ_e) of -9 (-13) K are observed. The position[5] of the θ_v and θ_e minimum is well to the rear ($\sim$10 km west) of the maximum reflectivity within the main core. Latent chilling owing to the evaporation of rain and melting of graupel or hail primarily contributes to this thermodynamic footprint. Furthermore, there is a clear thermal trough along the maximum reflectivity axis (along roughly $y = 10$ km, Figs. 3a–c) that sharpens with increasing rearward distance/time. Since copious hailfall was observed by Stick-Net crews and other field participants in this region, a portion of this observed deficit is also attributable to the cooling by fallen hail.[6]

The D2NT deployment features a similar position of the minimum thermodynamic perturbations to the left and rear of the low-level mesocyclone (Figs. 4a,b). Over the storm scale, the extrema of these perturbations are found to be weaker than D1WT, with minimum perturbations of -7 (-11) K in θ_v (θ_e). However, near the position of the radar-identified low-level mesocyclone (the origin in Figs. 3a,b and 4a,b), deficits in θ_e are more

---

[5] The position of features in the moisture and, to a lesser extent, temperature fields is naturally affected by the response time of the instrumentation (see section 2).

[6] To crudely estimate the impact of such cooling, a bulk aerodynamic formula for buoyancy flux ($\overline{w'T'}$) at the surface is used:

$$\overline{w'T'}\big|_0 = C_h V(T_{hail} - T_{air})P,$$

where C_h, a dimensionless bulk transfer coefficient, is taken to be 3×10^{-3} following observations of a melting ice surface by Braithwaite (2009); V, the wind speed, is set to $7.5\,m\,s^{-1}$, a magnitude representative of StickNet measurements within and to the rear of the heaviest core precipitation (Fig. 3c); the temperature of the melting hail (T_{hail}) is set to 273.15 K; T_{air}, the air temperature at measurement level ($\sim$2.5 m AGL) equals 291.15 K; and P is the fractional ground coverage of fallen hail, estimated to be 0.1 from photographs and the recollection of the StickNet crew. From the equation in footnote 6, the surface buoyancy flux is calculated to be $-0.04\,K\,m\,s^{-1}$. A vertical buoyancy flux divergence ($4 \times 10^{-4}\,K\,s^{-1}$) is calculated assuming a linear increase in buoyancy flux from a minimum ($-0.04\,K\,m\,s^{-1}$) near the surface to a value of zero at 100 m AGL, an assumed depth of influence from this conductional cooling. For a 30-min (1800 s) span, similar to the span of StickNet measurement within and to the rear of the most intense core precipitation, the temperature change is -0.72 K, which is of similar magnitude to the increase in θ_v deficit for the hail-affected probes (Fig. 3a; probe ID 17A and 24B) over nearby stations within the cold pool.
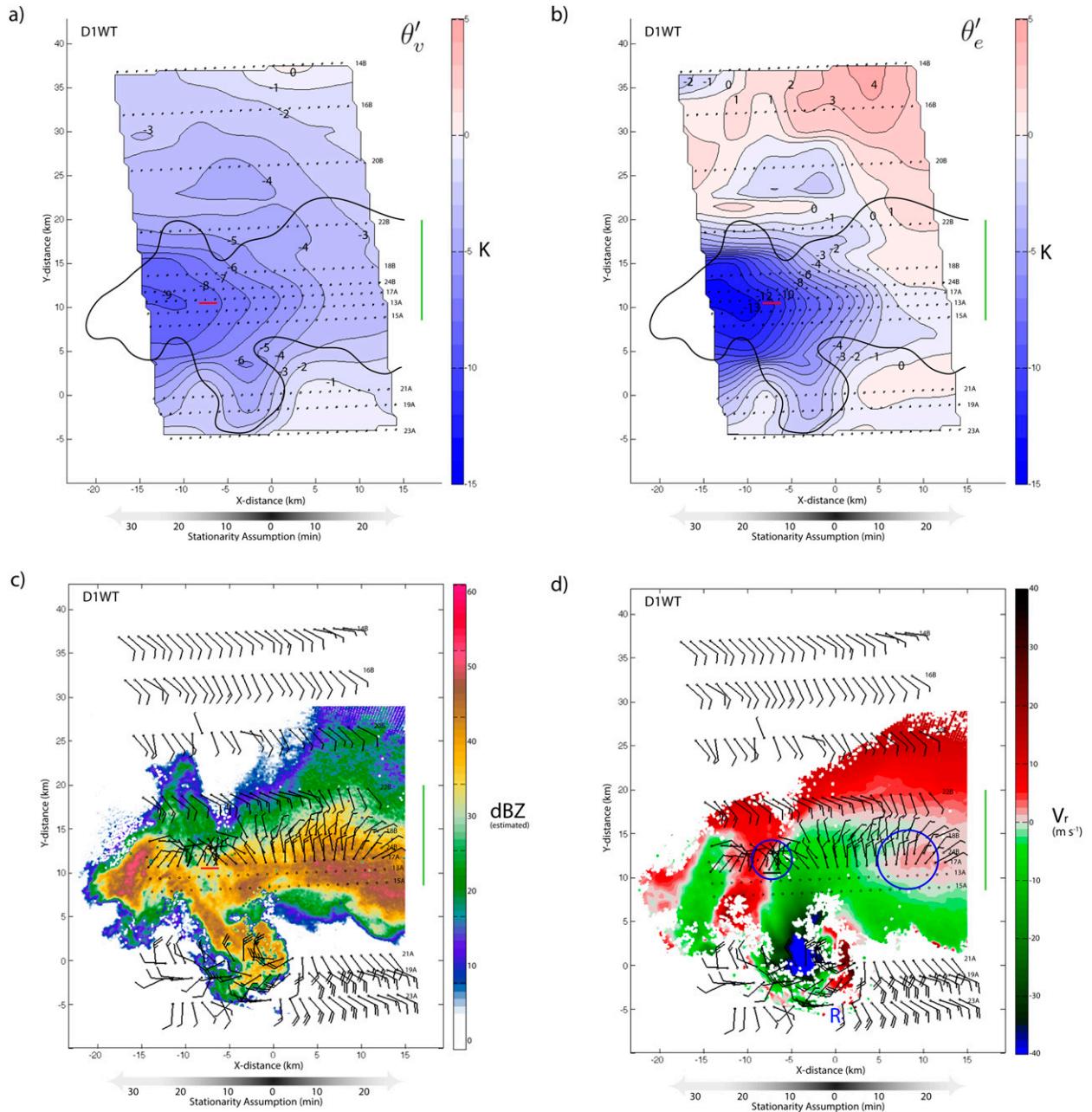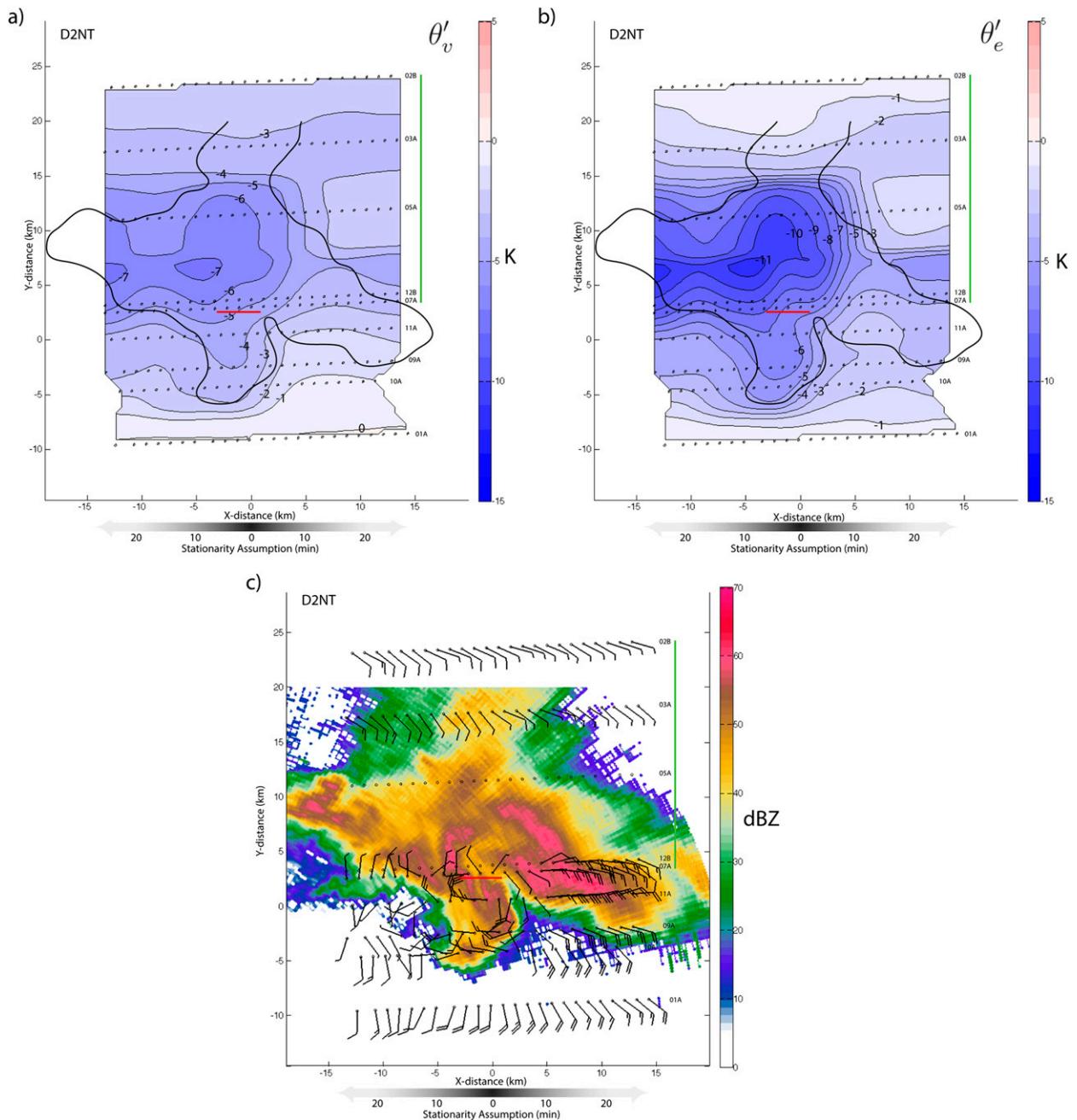
FIG. 3. Analyzed (a) perturbation virtual potential temperature (K, shaded and contoured) and (b) perturbation equivalent potential temperature (K, shaded and contoured). (c) 10-s averaged ground-relative winds (barbs, kt, plotted every 120 s; full barb = 10 kt, half barb = 5 kt; 1 kt = 0.5144 m s^{-1}) and DOW6 radar reflectivity [dBZ (estimated), shaded], and (d) as in (c), but for DOW6 radial velocity (m s^{-1}, shaded) valid at 2330 UTC 18 May 2010. The 30 dBZ (estimated) contour from DOW6 is shown in (a) and (b). The period of StickNet analysis corresponds to deployment D1WT, 2303–2353 UTC 18 May 2010. The origin (0, 0) is at the location of the maximum inferred vertical vorticity (described in text). Stations with no wind barbs indicate probes providing only thermodynamic data. The green vertical line in each panel brackets the probes presented in Fig. 10a; probe ID is indicated. The varying restrictiveness of the stationarity assumption is indicated at the bottom (see section 3). The blue circles in (d) denote regions of in situ and radar comparison referred to in section 2. The location of DOW6 is indicated by the blue "R." The short, solid red line [black line in (d)] near $x = -7$, $y = -10$ km denotes the period for the time trace in Fig. 11a.

FIG. 4. Analyzed (a) perturbation virtual potential temperature (K, shaded and contoured), (b) perturbation equivalent potential temperature (K, shaded and contoured), and (c) 10-s-averaged ground-relative winds (barbs, kts) and SMART-R1 radar reflectivity (dBZ, shaded) valid at 0024 UTC 19 May 2010. The 45-dBZ contour from SMART-R1 is shown in (a) and (b). The period of StickNet analysis corresponds to deployment D2NT, 0000–0050 UTC 19 May 2010. The origin (0, 0) is at the location of the maximum inferred vertical vorticity (described in text). The green vertical line in each panel brackets the probes presented in Fig. 10b; the probe ID is indicated. The varying restrictiveness of the stationarity assumption is indicated at the bottom (see section 3). The short, solid red line near $x = -2$, $y = 2$ km denotes the period for the time trace in Fig. 11b.

significant for D2NT [$\theta'_e \sim -2$ (-6) K for D1WT (D2NT)], suggesting that air parcels entering the low-level mesocyclone from the surface in the D2NT case are less potentially buoyant and, therefore, less prone to

strong vertical acceleration within the updraft (assuming the overlying atmosphere did not change significantly between these two deployments). However, θ_v deficits are similar (~ -3.5 K) at the origin of the two cases,
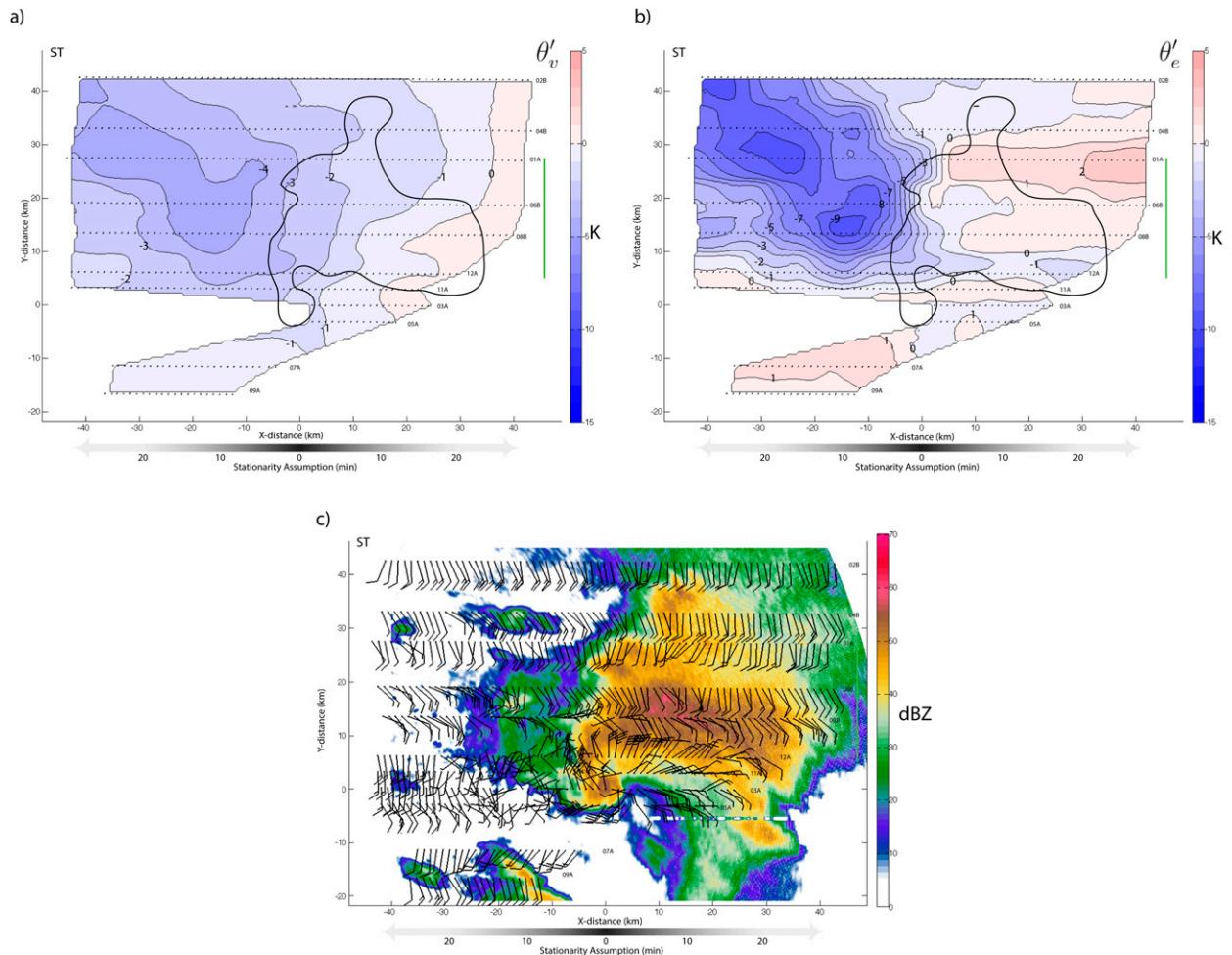
FIG. 5. Analyzed (a) perturbation virtual potential temperature (K, shaded), (b) perturbation equivalent potential temperature (K, shaded), and (c) 10-s-averaged ground-relative winds (barbs, kt, plotted every 50 s) and KOUN radar reflectivity (dBZ, shaded) valid at 2316 UTC 10 May 2010. The 45-dBZ contour from KOUN is shown in (a) and (b). The period of StickNet analysis corresponds to deployment ST, 2250–2350 UTC 10 May 2010. The origin (0, 0) is at the location of the maximum inferred vertical vorticity (described in text). The green vertical line in each panel brackets the probes presented in Fig. 10c; the probe ID is indicated. The varying restrictiveness of the stationarity assumption is indicated at the bottom (see section 3).

indicating similar negative buoyancy in the lower levels of each storm. Similar to D1WT, a thermal trough appears near and to the rear of the axis of highest reflectivity, where noteworthy hailfall had occurred. The first author observed hailstones in excess of 6 cm in diameter and a shallow hail fog upon pickup of the two probes recording this deficit (approximately 60 min after the storm had passed); substantial damage occurred to the anemometer of one of these probes.

Of the three cases presented, the ST deployment reveals the weakest storm-scale θ_v and θ_e deficits (Figs. 5a,b), with θ_v (θ_e) perturbations of -4 (-9) K evident in the rear-left flank of the storm. Near the position of the low-level mesocyclone and tornado, however, these deficits are practically negligible—even a weak surplus in θ_e is

analyzed in the mesocyclone region and near-field inflow, similar in position to that identified by Skinner et al. (2011) for a StickNet intercept of a supercell near Perryton, Texas, in 2007. These findings are directly in line with those of others (e.g., Markowski et al. 2002; Grzych et al. 2007; Hirth et al. 2008; Lee et al. 2012) who find strongly tornadic (nontornadic) mesocyclones to be associated with weak (strongly negative) temperature perturbations.

b. Thermodynamic and kinematic character of the forward flank

The bulk thermodynamic characteristic of the forward flank follows the same progression as reported in the previous section: the WT and NT cases feature larger deficits in θ_v and θ_e compared to the ST case; however,
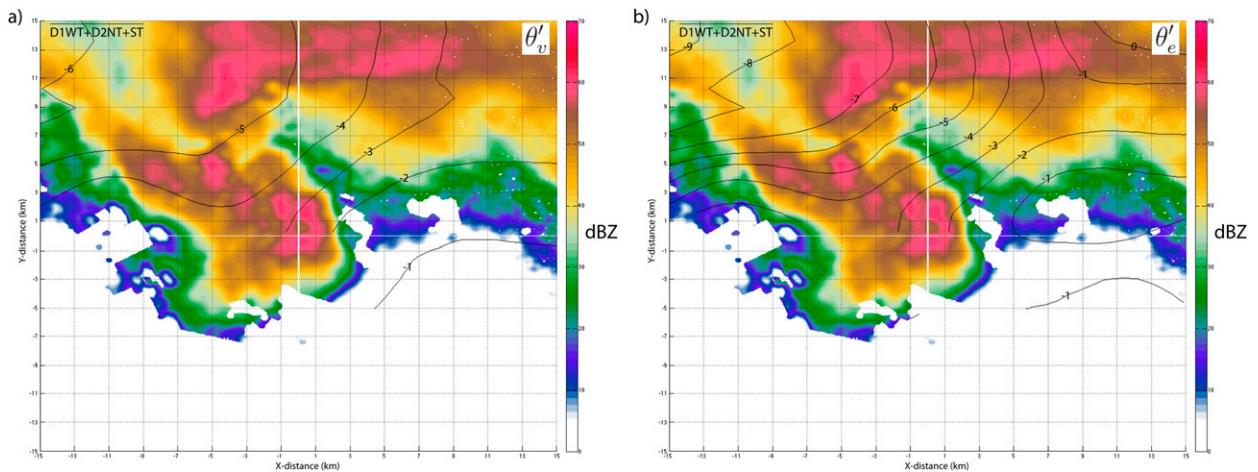
FIG. 6. Three-deployment composite (a) perturbation virtual potential temperature (K, contoured) and (b) perturbation equivalent potential temperature (K, contoured). Reflectivity (dBZ, shaded) represents a three-deployment composite. The origin (0, 0) is at the location of the maximum inferred vertical vorticity (described in text).

the NT case was somewhat warmer than WT. In fact, the maximum deficit in θ_v for WT within the forward flank (−6 K) is the same as the consensus of the five nontornadic forward-flank samples obtained with mobile mesonet in VORTEX1 (Shabbott and Markowski 2006).

Composite θ_v and θ_e plots, created by averaging the perturbations from all three cases (Figs. 6a,b), show a clear monotonic increase in the θ_v and θ_e deficits from the inflow region east of the mesocyclone to the rear of the average main core position. The mean distribution reveals a relatively weak θ_v gradient (with contours oriented roughly from west to east) near the forward-flank reflectivity gradient (FFRG), and another, stronger gradient (with contours oriented roughly from

southwest to northeast) within the precipitation core (further discussed in section 5d).

Differencing of the D1WT and D2NT fields allows a direct comparison of the storm-scale structure for a weakly tornadic and nontornadic phase of the 18 May 2010 storm, with roughly the same background environment. Owing in large part to the differences in position of the core precipitation relative to the low-level mesocyclone, the perturbation virtual potential temperature gradient to the north and east of the low-level mesocyclone (Fig. 7a) is oriented largely toward the southeast, a direction consistent with a component of streamwise baroclinic vorticity tendency for typical trajectories approaching the low-level mesocyclone
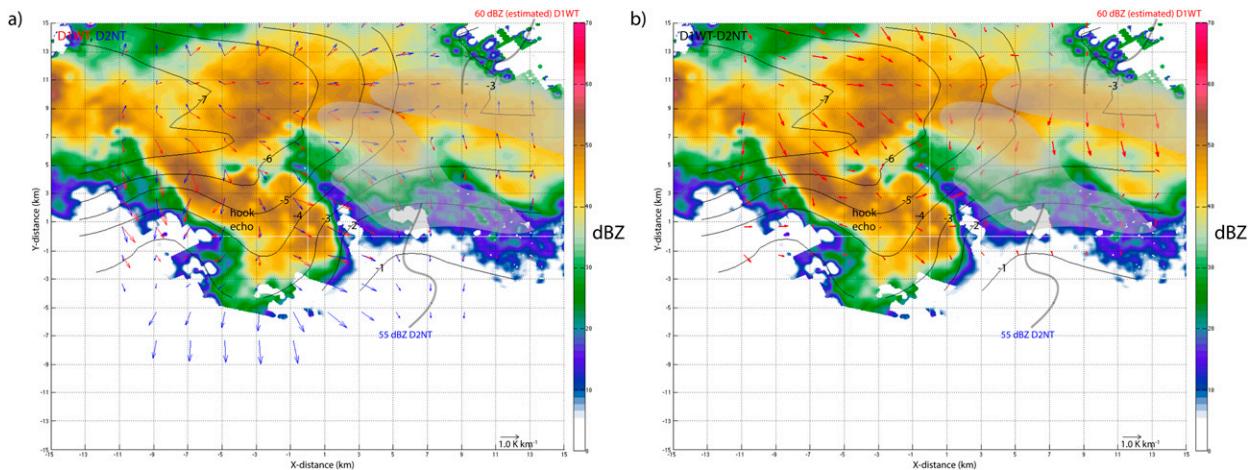

FIG. 7. (a) Gradient vectors of virtual potential temperature (K km^{-1}, reference vector in lower-right corner) for deployments D1WT (red) and D2NT (blue), and (b) the vector difference D1WT − D2NT. Two-case (D1WT, D2NT) composite radar reflectivity (shaded) and perturbation virtual potential temperature (contoured) are indicated. The gray shading denotes regions of DOW6 reflectivity in excess of 60 dBZ (estimated) for deployment D1WT (cf. Fig. 3c) and SMART-R1 reflectivity in excess of 55 dBZ for deployment D2NT (cf. Fig. 4c).
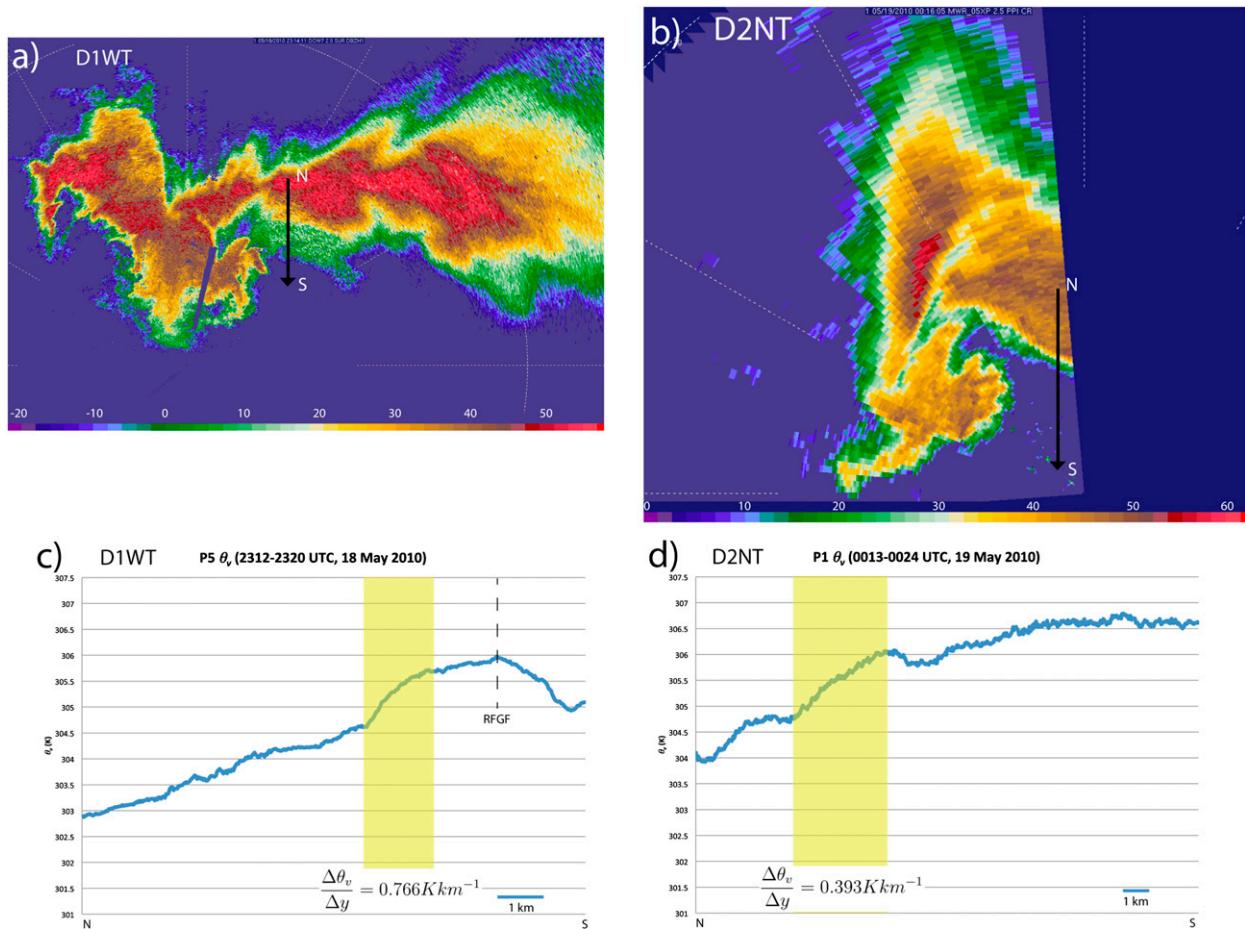
FIG. 8. (a) DOW7 2.0° elevation radar reflectivity [shaded, dBZ, scale at bottom (estimated)] valid at 2314 UTC 18 May 2010; (b) MWR-05XP 2.5° elevation radar reflectivity valid at 0016 UTC 19 May 2010; (c),(d) time series of virtual potential temperature (K) as recorded by PSU/NSSL mobile mesonet probe 5 during 2312–2320 UTC, and probe 1 during 0013–0024 UTC 19 May 2010, respectively. Letters "N" (north) and "S" (south) denote the endpoints of the traverse. The yellow shaded region denotes the period over which the virtual potential temperature gradient is calculated. The location of the rear-flank gust front (RFGF) passage in (a) is indicated.

from the northeast [e.g., as repeatedly produced in the simulations and observational analyses of Klemp and Rotunno (1983); Rotunno and Klemp (1985); Wicker and Wilhelmson (1995); Beck and Weiss (2013); Kosiba et al. (2013); Markowski et al. (2012b); Dahl et al. (2014); similarly, storm-relative winds for these deployments are from the northeast in this same area northeast of the low-level mesocyclone (not shown)]. Differences in θ_v gradients between D1WT and D2NT are noticeable across the FFRG and the eastern portion of the hook echo (Fig. 7b), with magnitudes of approximately 0.6–1.0 K km^{-1}, increasing to nearly 1.5 K km^{-1} toward the rear of the core. The θ_v gradients in the region of the FFRG were confirmed using individual mobile mesonet transects from 2312 to 2320 UTC (near the time of the D1WT deployment, Fig. 8a) and 0013–0024 UTC (near the time of the D2NT deployment, Fig. 8b). The calculated latitudinal gradient of θ_v for deployment D1WT

(D2NT) is 0.766 (0.393) K km^{-1} (Figs. 8c,d), in line with the aforementioned gradients derived from StickNet. The finding of a stronger baroclinic zone across the FFRG in this particular tornadic case is in disagreement with the conclusion of Shabbott and Markowski (2006), who found that forward-flank outflow features larger horizontal buoyancy gradients in nontornadic supercells.

Perhaps the most striking disparity between the D1WT and D2NT analyses relates to the measured ground-relative winds (Figs. 3c and 4c) within the forward flank. Winds were easterly throughout this region during the D2NT deployment. However, this region within the D1WT deployment, albeit farther to the north within the core precipitation, featured much more strongly backed (northerly) winds, revealing a strongly diffluent region within the forward flank, approximately 15–20 km to the north and northeast of the low-level mesocyclone. The ST case (Fig. 5c) also shows northerlies in the main core, with
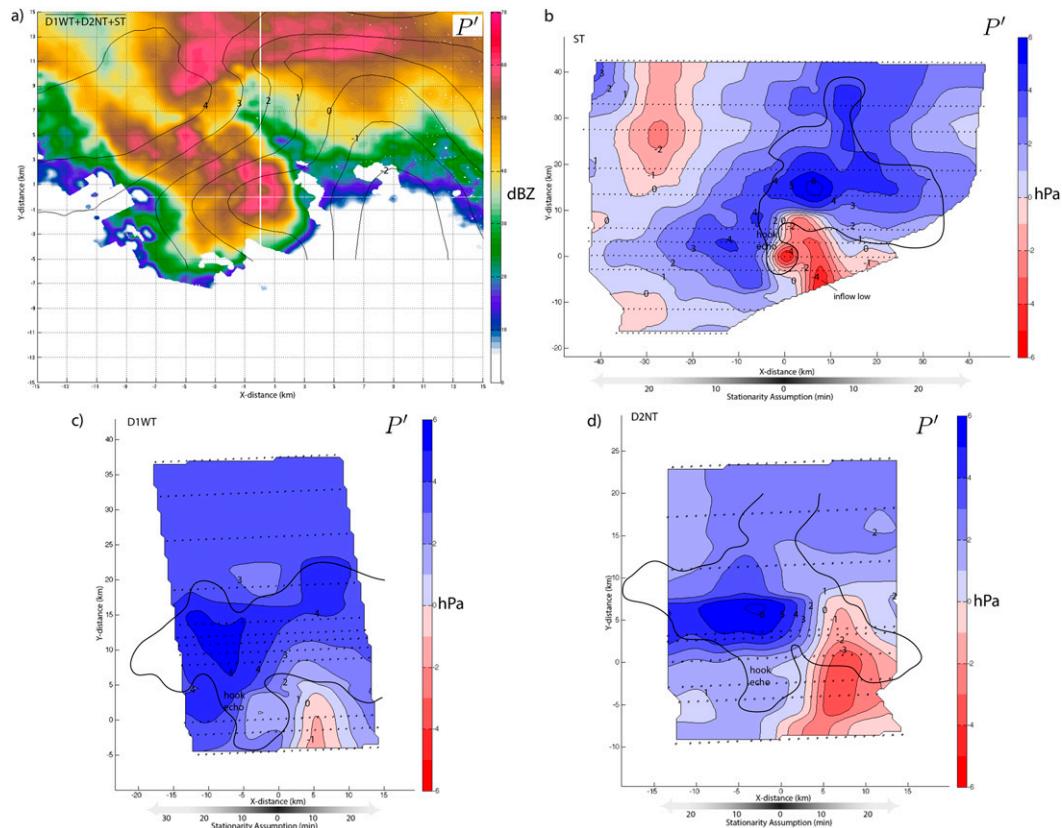
FIG. 9. (a) Three-deployment composite, and (b) ST, (c) D1WT, and (d) D2NT perturbation pressure (hPa, contoured). In (a), the three-deployment composite radar reflectivity (shaded) is shown. In (b)–(d), the ragged black outline represents the same contour of constant reflectivity as presented in Figs. 3–5.

diffluence to the north, and confluence to the south along the FFRG. The D1WT and ST wind analyses qualitatively look more similar to the traditional notion of a forward-flank downdraft and gust front as presented by Lemon and Doswell (1979).

c. Pressure

All three cases share some similar features in the perturbation pressure field. A ubiquitous deficit in pressure, 2 hPa in the composite analysis (Fig. 9a), is evident in a position 5–10 km east and southeast of the low-level mesocyclone. This structure is most clearly displayed in the ST case (Fig. 9b), with a wide area of 3–4 hPa deficits curving northwestward from a relative minimum at ~[8, −5], then southwestward to the position of the low-level mesocyclone and tornado at the origin (maximum observed deficit in the StickNet time series is ~17 hPa). The sampling for D1WT is coarser, but the analysis (Fig. 9c) still shows a weak trough of lower pressure through the low-level mesocyclone, in addition to the stronger deficit farther southeast. The D2NT sample (Fig. 9d) shows very little evidence of a pressure trough

within the low-level mesocyclone but does indicate a prominent minimum farther east. In combination with the larger θ_v and θ_e deficits near this position, the limited response in pressure may indicate that the low-level mesocyclone was occluded and decaying.

Farther within the precipitation core, the ST case demonstrates a clearly different pattern of pressure perturbation compared to both the D1WT and D2NT cases. Specifically, the ST case is the only to reveal a bounded local maximum in pressure within the forward flank, approximately 5 hPa above the base state, extending over an approximately 50 km^2 area within the forward-flank precipitation. Combined with the aforementioned low associated with the updraft, a feature similar to the "inflow low" derived by Davies-Jones (2002), the pressure gradient points almost due northward and exceeds 0.8 hPa km^{-1} north of the FFRG. In the D1WT and D2NT cases, the pressure gradient is weaker and directed more northwestward, as maximum surpluses occur to the rear of the storm. The D2NT case is the only one of the three to show no extension of the core pressure maximum into the hook echo region.
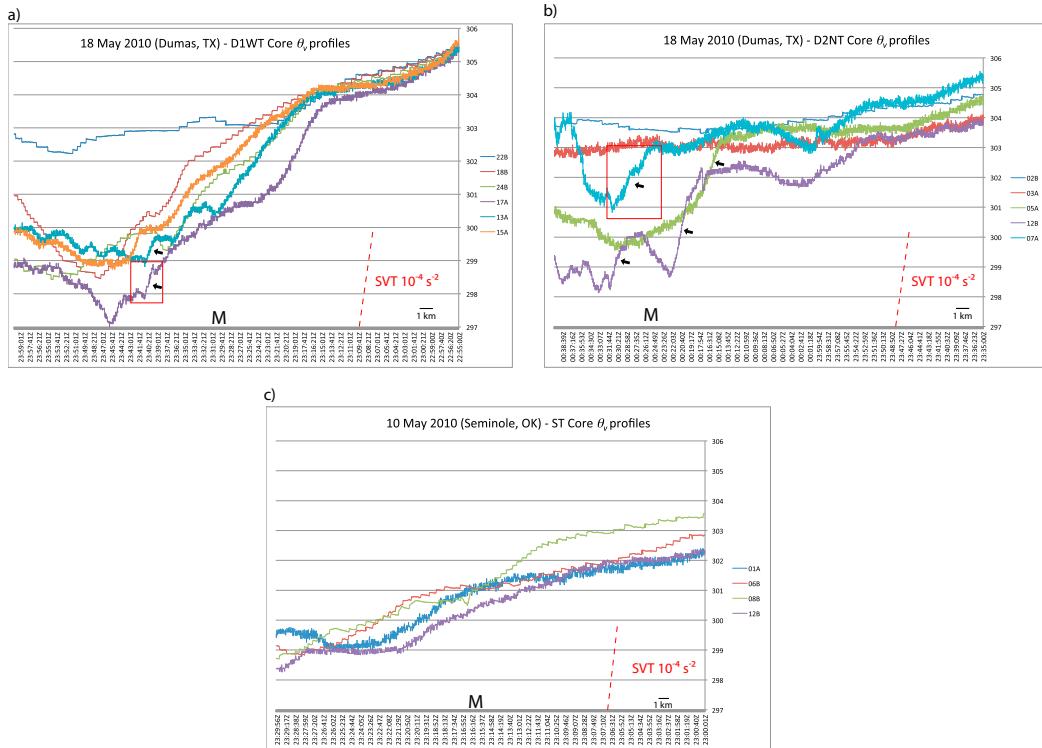
FIG. 10. A reverse time series of virtual potential temperature (K) from StickNet deployments (a) D1WT, (b) D2NT, and (c) ST. StickNet Probe IDs are listed from north to south in the legend on the right-hand side and further indicated in Fig. 3a (D1WT), Fig. 4a (D2NT), and Fig. 5a (ST). The dashed red line in the lower-right-hand corner denotes a virtual potential temperature gradient of 3 K km^{-1}, corresponding to a solenoidal vorticity tendency of 1×10^{-4} s^{-2} [for parcels translating normal to storm motion, following from the scaling of Klemp and Rotunno (1983)]. The letter "M" indicates for each case the time when the maximum inferred vertical vorticity is at the same longitude as the probes. Arrows point to features discussed in the text. Red boxes in (a) and (b) denote the period of the time traces in Figs. 11a and 11b, respectively.

d. Baroclinic zones to the left of the updraft

A recent study by Beck and Weiss (2013) has identified local regions on both the forward and left sides of the updraft where near-surface baroclinic vorticity tendency {defined in a natural coordinate system as $\partial/\partial z[\alpha(\partial p/\partial n)]$, where α is the specific volume} can be significant $[O(\sim 10^{-4})$ s$^{-2}]$, owing primarily to bursts of hydrometeor loading and latent chilling. Individual time series of StickNet data from the three cases were inspected to identify if similar tendencies were observable, recognizing the likely impact of the instrumentation response on underestimating these gradients (Table 2).

The trend in θ_v for probes within the forward flank (to the east of the longitude of the low-level mesocyclone) of the selected cases is largely monotonic (Figs. 10a–c), with a steady decrease in θ_v noted throughout each of the samples (cf. Fig. 6a). Deployment D1WT features the strongest such tendency, approximately double that of ST. Though the magnitude of these θ_v gradients to the north of the low-level mesocyclone is predominantly

weaker than the $O(\sim 10^{-4})$ s^{-2} reported by Beck and Weiss (2013), there exist specific regions where the intensity of the gradients is similar. The D2NT time series contains a region of equivalent width 2 km (around 0020 UTC) where the baroclinic tendency exceeds 10^{-4} s^{-2} at probe 12B (Fig. 10b). As identified earlier, this probe was at the location of KAMA-measured base reflectivity in excess of 70 (65) dBZ for 3 (7) min prior to the observation, and observed severe hail on the ground at 60 min following storm passage. It is plausible that— beyond the evaporational cooling of rain—both the melting of falling hail and the conductional cooling afforded by grounded hail may have contributed to the sharp air density gradient, though it is unknown how quickly this latter mechanism could be realized at measurement height. Similar, slightly less intense gradients are sampled by probes 05A and 02B within 10 min (~ 6 km) of that indicated by probe 12B.

To the rear (northwest) side of the low-level mesocyclone, both the D1WT and D2NT deployments contain zones of near $O(\sim 10^{-4})$ s^{-2} baroclinic vorticity
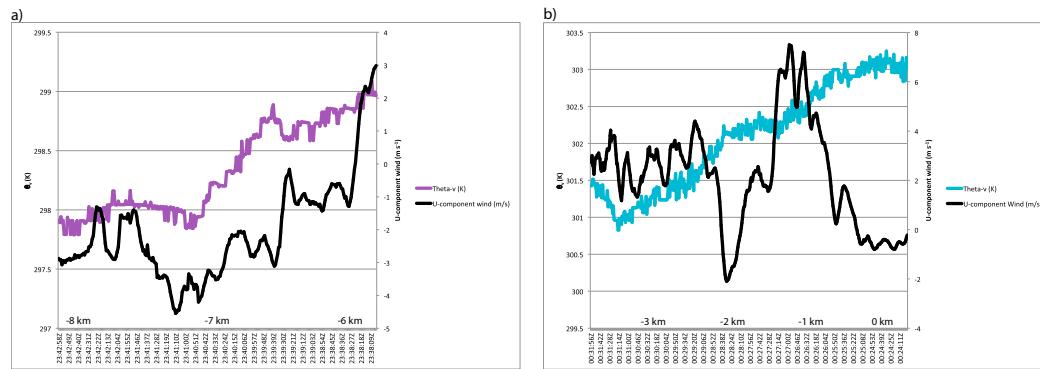
FIG. 11. A reverse time series of virtual potential temperature (colored trace, K) and a 9-s moving average of u-component wind (black trace, m s^{-1}) from (a) probe 17A in the D1WT deployment (refer to red line in Figs. 3a–d and red box in Fig. 10a) and (b) probe 07A during the D2NT deployment (refer to red line in Figs. 4a–c and red box in Fig. 10b). The position labels along the bottom axis of (a) and (b) correspond to the x-coordinate position in Figs. 3a–d and Fig. 4c, respectively.

generation (Figs. 10a and 10b). In D1WT, these zones occupy narrow windows of time (approximately 1 km in equivalent width) near 2340 UTC at probes 13A and 17A. Probe 15A reveals a similar gradient near 2342 UTC (the probe is slightly east of the longitude of probes 13A and 17A, which could well explain the discrepancy in time). Research is ongoing into the association of these thermodynamic inflections with a low-reflectivity ribbon (Kosiba et al. 2013; Snyder et al. 2013), which was observed by mobile radar near the locations of these probes. Similar zones are present in the same low-level mesocyclone-relative positions for 07A and 12B probes in deployment D2NT.

To further assess whether these observed baroclinic zones are consistent with the notion of the left-flank convergence boundaries (LFCBs) of Beck and Weiss (2013), the evolution of the u component of the wind is considered across two of the stronger zones, one for each deployment, where anemometry was not damaged by hailfall. The results are mixed. The region identified by probe 17A during D1WT actually features a predominantly *diffluent* flow (Fig. 11a), whereas individual narrow zones of strong confluence and diffluence are evident in the data from probe 07A from the D2NT deployment (Fig. 11b), more similar to the transient bursts of outflow that precede the establishment of the dominant LFCB in the simulations of Beck and Weiss (2013).

6. Summary and discussion

In situ observations from three separate VORTEX2 StickNet deployments are presented. The two analysis periods from 18 May 2010 cover a supercell thunderstorm in the northern Texas Panhandle, contrasting a weak tornadic phase near Dumas, Texas, with a nontornadic

period approximately 20 km to the east. A separate strongly tornadic case from Seminole, Oklahoma, on 10 May 2010 is used for further comparison.

Though the environment is similar between the two 18 May 2010 deployments, there are some differences evident in the storm-scale thermodynamic presentation. The vector difference in $\mathbf{V}_h \theta'_v$ between the NT and WT cases (weakly tornadic minus nontornadic) largely points southward within the average position of the FFRG across the two cases, southeastward in the rear upshear region of the core, and eastward along the inflow side of the hook echo (Fig. 7b). These differences are partly attributable to the position of the core precipitation relative to the radar-level mesocyclone for each case, the D1WT case featuring precipitation farther to the left, looking downshear. The magnitudes of these differences are fairly modest, approximately 0.5 K km^{-1} on average across the three aforementioned sections. However, the orientation of the vectors is consistent with a greater streamwise baroclinic tendency in the weakly tornadic case compared to the nontornadic case,[7] for typical inbound trajectories from the northwest through northeast as demonstrated in a number of previously cited numerical simulations. Using the scale analysis of Klemp and Rotunno (1983), parcels

---

[7] The acquisition of streamwise vorticity, and the resultant reorientation of vorticity vectors from their environmental alignment, indicates the preference for these parcels to contribute to the circulation of the low-level mesocyclone. However, recent studies by Markowski and Richardson (2014) and Dahl et al. (2014) identify that, in their simulations, even crosswise horizontal vorticity can quickly become streamwise through crosswise-to-streamwise exchange as parcels moving westward through the forward flank turn southward to approach the low-level mesocyclone from the north.

moving through these strongest baroclinic zones (perpendicular to the density gradient) would acquire additional horizontal vorticity of approximately $1.6 \times 10^{-3}\,\mathrm{s}^{-1}\,\mathrm{km}^{-1}$.[8] A 10-km extent of such a trajectory would therefore yield $O(\sim 10^{-2})\,\mathrm{s}^{-1}$ vorticity, a portion of which would be tilted into the vertical as parcels descend in the downdraft region, and subsequently stretched in the updraft.[9]

The θ_v and θ_e deficits are uniformly weaker throughout the ST case in comparison to either of the Dumas deployments, a finding consistent with the consensus of previous direct in situ observations (e.g., Markowski et al. 2002; Grzych et al. 2007; Hirth et al. 2008; Skinner et al. 2011; Lee et al. 2012). The magnitudes of $\mathbf{V}_h\theta_v'$, in turn, are much weaker throughout the storm, which, when considering the previous comparison of baroclinity for the D1WT and D2NT intercepts, may reveal the paradoxical role of cold pools in modulating near-surface vertical vorticity in these particular storms. The D2NT case, for instance, shows much greater potential baroclinic vorticity tendency (provided parcels actually traverse these baroclinic zones) than the ST case, which highlights the relative importance of the magnitude of buoyancy in the outflow of tornadic storms. However, in spite of the weak observed thermodynamic gradients, the ST case best demonstrates a bounded maximum in pressure within the forward-flank precipitation and an identifiable northerly component to the ground-relative winds near the forward-flank reflectivity gradient, both features that are consistent with the notion of outflow originating from the precipitation core [e.g., the "starburst" pattern of streamlines associated with the forward-flank downdraft in Lemon and Doswell (1979)]. In addition to the association with streamwise baroclinic vorticity production, the predominantly northerly component of the ground-relative flow within the forward-flank outflow in the WT and ST cases is also consistent with the frictional generation of (eastward directed) horizontal vorticity near the surface, similar to that found behind a forward-flank convergence boundary by Schenkman et al. (2014) in simulations of the 8 May 2003 supercell near Oklahoma City, Oklahoma.

The somewhat incongruous relationship between the surface thermodynamic and pressure/wind field, the fact that the maximum in pressure and minimum in θ_v are not aligned, suggests that the pressure maximum within the precipitation core is either attributable to nonhydrostatic effects or virtually cooler air aloft that is not present in the surface observing network. If the explanation is solely attributable to the latter of these, then surface pressure measurements could be a basis for the identification of baroclinic zones aloft, though additional information would be required to ensure such virtual potential temperature gradients are largely horizontal and occurring in layers traversed by the air parcels of interest. It is also possible that the horizontal accelerations resulting from these pressure perturbations can be influential in the conversion from crosswise to streamwise vorticity, per the "river-bend effect" described by Davies-Jones et al. (2001). The nontornadic D2NT sample is the only one not to show an extension of the pressure surplus from the core toward the rear flank. Though greater θ_v deficits can be found to the rear of D1WT compared to D2NT, perhaps allowing for a hydrostatic explanation for the discrepancy in pressure perturbation, the presence of a clear cyclonically curved pressure ridge west of the low-level mesocyclone in the ST case—a case with small θ_v deficits throughout the storm—cannot be supported in a similar manner. As the pressure excess in ST clearly traces the expected region of subsiding air within the storm, it seems plausible that the pressure excess is tied to a fundamental characteristic of these downdraft regions. One possible explanation relates pressure excesses to the stagnation of descending air upon contact with the surface. Such a mechanism would imply that RFD deceleration at the surface was weaker in the D2NT case than either D1WT or ST, which could be tied to the magnitude of the downdraft and/or the inclination of trajectories approaching the surface. With no dual-Doppler trajectory analyses to compare across the three cases, future work will invoke model-based analyses to determine the trajectories of air parcels within each RFD.

Recent simulations by Beck and Weiss (2013) suggest that narrow corridors of strong baroclinic vorticity tendency can extend into the rear portion of the forward flank, well rearward of the FFRG where one might traditionally expect these strongest baroclinic zones to exist (Lemon and Doswell 1979; Klemp and Rotunno 1983). A motivation for this study is to pursue whether

---

[8] Without the capability for material circuit analysis, it is impossible to know to what extent parcels reside within baroclinic zones for either deployment. This comparison of D1WT and D2NT necessarily supposes that the mesocyclone-relative distribution of inbound trajectories is identical between the cases, and that at least some of these parcels in D1WT travel within the regions of stronger streamwise baroclinic tendency to have a meaningful impact on the realized low-level vertical vorticity.

[9] As stated by Davies-Jones and Brooks (1993), descent within the rear-flank downdraft is required for baroclinic vorticity generation to produce "slippage" between the trajectory and vorticity vector, which subsequently produces vertical vorticity as the trajectory approaches the surface. It is recognized that the baroclinic zones presented in this study are necessarily at the surface, not within the descending air. It is, therefore, assumed that the buoyancy minimum extends vertically from the surface [e.g., the evolution of vortex rings presented by Markowski et al. (2008, see their Fig. 19)].

such regions are actually observed and not merely an artifact of (e.g., the microphysical parameterizations chosen for such simulations). Despite the unavoidable weakening of observed thermodynamic gradients owing to the time constant of in situ instrumentation (Table 2), the D1WT and D2NT deployments analyzed for this study show narrow zones of baroclinic tendency similar to that reported by Beck and Weiss (2013), on the order of ~1 km wide and positioned to the north and west of the low-level mesocyclone. Analysis of the u-component wind across these zones reveals narrow corridors of confluence and diffluence, similar to the bursts of outflow that precede the development of an established LFCB in the simulations of Beck and Weiss (2013). As such, it is suggested that these particular baroclinic zones in the D2NT deployment might be fairly transient in position and magnitude. Research is ongoing on the structure and origin of these zones.

REFERENCES

Adlerman, E. J., K. K. Droegemeier, and R. Davies-Jones, 1999: A numerical simulation of cyclic mesocyclogenesis. *J. Atmos. Sci.,* **56,** 2045–2069, doi:10.1175/1520-0469(1999)056<2045:ANSOCM>2.0.CO;2.

Barnes, S. L., 1964: A technique for maximizing details in numerical weather map analysis. *J. Appl. Meteor.,* **3,** 396–409, doi:10.1175/1520-0450(1964)003<0396:ATFMDI>2.0.CO;2.

Beck, J., and C. C. Weiss, 2013: An assessment of low-level baroclinity and vorticity within a simulated supercell. *Mon. Wea. Rev.,* **141,** 649–669, doi:10.1175/MWR-D-11-00115.1.

Biggerstaff, M. I., and Coauthors, 2005: The Shared Mobile Atmospheric Research and Teaching Radar: A collaboration to enhance research and teaching. *Bull. Amer. Meteor. Soc.,* **86,** 1263–1274, doi:10.1175/BAMS-86-9-1263.

Bolton, D., 1980: The computation of equivalent potential temperature. *Mon. Wea. Rev.,* **108,** 1046–1053, doi:10.1175/1520-0493(1980)108<1046:TCOEPT>2.0.CO;2.

Braithwaite, R. J., 2009: Calculation of sensible-heat flux over a melting ice surface using simple climate data and daily measurements of ablation. *Ann. Glaciol.,* **50,** 9–15, doi:10.3189/172756409787769726.

Brandes, E. A., 1978: Mesocyclone evolution and tornadogenesis: Some observations. *Mon. Wea. Rev.,* **106,** 995–1011, doi:10.1175/1520-0493(1978)106<0995:MEATSO>2.0.CO;2.

Dahl, J. M. L., M. D. Parker, and L. J. Wicker, 2014: Imported and storm-generated near-ground vertical vorticity in a simulated supercell. *J. Atmos. Sci.,* **71,** 3027–3051, doi:10.1175/JAS-D-13-0123.1.

Davies-Jones, R., 1984: Streamwise vorticity: The origin of updraft rotation in supercell storms. *J. Atmos. Sci.,* **41,** 2991–3006, doi:10.1175/1520-0469(1984)041<2991:SVTOOU>2.0.CO;2.

——, 2002: Linear and nonlinear propagation of supercell storms. *J. Atmos. Sci.,* **59,** 3178–3205, doi:10.1175/1520-0469(2003)059<3178:LANPOS>2.0.CO;2.

——, and H. Brooks, 1993: Mesocyclogenesis from a theoretical perspective. *The Tornado: Its Structure, Dynamics, Prediction, and Hazards, Geophys. Monogr.,* Vol. 79, Amer. Geophys. Union, 105–114.

——, R. J. Trapp, and H. B. Bluestein, 2001: Tornadoes and tornadic storms. *Severe Convective Storms, Meteor. Monogr.,* No. 50, Amer. Meteor. Soc., 167–221.

Dowell, D. C., and H. B. Bluestein, 2002a: The 8 June 1995 McLean, Texas, storm. Part I: Observations of cyclic tornadogenesis. *Mon. Wea. Rev.,* **130,** 2626–2648, doi:10.1175/1520-0493(2002)130<2626:TJMTSP>2.0.CO;2.

——, and ——, 2002b: The 8 June 1995 McLean, Texas, storm. Part II: Cyclic tornado formation, maintenance, and dissipation. *Mon. Wea. Rev.,* **130,** 2649–2670, doi:10.1175/1520-0493(2002)130<2649:TJMTSP>2.0.CO;2.

Grzych, M. L., B. D. Lee, and C. A. Finley, 2007: Thermodynamic analysis of supercell rear-flank downdrafts from Project ANSWERS. *Mon. Wea. Rev.,* **135,** 240–246, doi:10.1175/MWR3288.1.

Hirth, B. D., J. L. Schroeder, and C. C. Weiss, 2008: Surface analysis of the rear-flank downdraft outflow in two tornadic supercells. *Mon. Wea. Rev.,* **136,** 2344–2363, doi:10.1175/2007MWR2285.1.

Klemp, J. B., and R. Rotunno, 1983: A study of the tornadic region within a supercell thunderstorm. *J. Atmos. Sci.,* **40,** 359–377, doi:10.1175/1520-0469(1983)040<0359:ASOTTR>2.0.CO;2.

Kosiba, K., J. Wurman, Y. P. Richardson, P. M. Markowski, P. Robinson, and J. Marquis, 2013: Genesis of the Goshen County, Wyoming, tornado on 5 June 2009 during VORTEX2. *Mon. Wea. Rev.,* **141,** 1157–1181, doi:10.1175/MWR-D-12-00056.1.

Lee, B. D., C. A. Finley, and T. M. Samaras, 2011: Surface analysis near and within the Tipton, Kansas, tornado on 29 May 2008. *Mon. Wea. Rev.,* **139,** 370–386, doi:10.1175/2010MWR3454.1.

——, ——, and C. D. Karstens, 2012: The Bowdle, South Dakota, cyclic tornadic supercell of 22 May 2010: Surface analysis of rear-flank downdraft evolution and multiple internal surges. *Mon. Wea. Rev.,* **140,** 3419–3441, doi:10.1175/MWR-D-11-00351.1.

Lemon, L. R., and C. A. Doswell III, 1979: Severe thunderstorm evolution and mesocyclone structure as

related to tornadogenesis. *Mon. Wea. Rev.,* **107,** 1184–1197, doi:10.1175/1520-0493(1979)107<1184:STEAMS>2.0.CO;2.

Majcen, M., P. Markowski, Y. Richardson, D. Dowell, and J. Wurman, 2008: Multipass objective analyses of Doppler radar data. *J. Atmos. Oceanic Technol.,* **25,** 1845–1858, doi:10.1175/2008JTECHA1089.1.

Markowski, P. M., and Y. P. Richardson, 2014: The influence of environmental low-level shear and cold pools on tornadogenesis: Insights from idealized simulations. *J. Atmos. Sci.,* **71,** 243–275, doi:10.1175/JAS-D-13-0159.1.

——, J. M. Straka, and E. N. Rasmussen, 2002: Direct surface thermodynamic observations within the rear-flank downdrafts of nontornadic and tornadic supercells. *Mon. Wea. Rev.,* **130,** 1692–1721, doi:10.1175/1520-0493(2002)130<1692:DSTOWT>2.0.CO;2.

——, Y. P. Richardson, E. Rasmussen, J. Straka, R. Davies-Jones, and R. J. Trapp, 2008: Vortex lines within low-level mesocyclones obtained from pseudo-dual-Doppler radar observations. *Mon. Wea. Rev.,* **136,** 3513–3535, doi:10.1175/2008MWR2315.1.

——, and Coauthors, 2012a: The pretornadic phase of the Goshen County, Wyoming, supercell of 5 June 2009 intercepted by VORTEX2. Part I: Evolution of kinematic and surface thermodynamic fields. *Mon. Wea. Rev.,* **140,** 2887–2915, doi:10.1175/MWR-D-11-00336.1.

——, and Coauthors, 2012b: The pretornadic phase of the Goshen County, Wyoming, supercell of 5 June 2009 intercepted by VORTEX2. Part II: Intensification of low-level rotation. *Mon. Wea. Rev.,* **140,** 2916–2938, doi:10.1175/MWR-D-11-00337.1.

Marquis, J., Y. P. Richardson, P. M. Markowski, D. C. Dowell, and J. Wurman, 2012: Tornado maintenance investigated with high-resolution dual-Doppler and EnKF analysis. *Mon. Wea. Rev.,* **140,** 3–27, doi:10.1175/MWR-D-11-00025.1.

Palmer, R. D., and Coauthors, 2011: Observations of the 10 May 2010 tornado outbreak using OU-PRIME: Potential for new science with high-resolution polarimetric radar. *Bull. Amer. Meteor. Soc.,* **92,** 871–891, doi:10.1175/2011BAMS3125.1.

Pauley, P. M., and X. Wu, 1990: The theoretical, discrete, and actual response of the Barnes objective analysis scheme for one- and two-dimensional fields. *Mon. Wea. Rev.,* **118,** 1145–1164, doi:10.1175/1520-0493(1990)118<1145:TTDAAR>2.0.CO;2.

Rotunno, R., 1981: On the evolution of thunderstorm rotation. *Mon. Wea. Rev.,* **109,** 577–586, doi:10.1175/1520-0493(1981)109<0577:OTEOTR>2.0.CO;2.

——, and J. Klemp, 1985: On the rotation and propagation of simulated supercell thunderstorms. *J. Atmos. Sci.,* **42,** 271–292, doi:10.1175/1520-0469(1985)042<0271:OTRAPO>2.0.CO;2.

Schenkman, A. D., M. Xue, and M. Hu, 2014: Tornadogenesis in a high-resolution simulation of the 8 May 2003 Oklahoma City supercell. *J. Atmos. Sci.,* **71,** 130–154, doi:10.1175/JAS-D-13-073.1.

Schroeder, J. L., and C. C. Weiss, 2008: Integrating research and education through measurement and analysis. *Bull. Amer. Meteor. Soc.,* **89,** 793–798, doi:10.1175/2008BAMS2287.1.

Shabbott, C. J., and P. M. Markowski, 2006: Surface in situ observations within the outflow of forward-flank downdrafts of supercell thunderstorms. *Mon. Wea. Rev.,* **134,** 1422–1441, doi:10.1175/MWR3131.1.

Skinner, P. S., C. C. Weiss, P. M. Markowski, and Y. P. Richardson, 2010: Intercomparison between mobile and stationary surface observing platforms in VORTEX2. *25th Conf. on Severe Local Storms,* Denver, CO, Amer. Meteor. Soc., P5.1. [Available online at https://ams.confex.com/ams/25SLS/techprogram/paper_176245.htm.]

——, ——, J. L. Schroeder, L. J. Wicker, and M. I. Biggerstaff, 2011: Observations of the surface boundary structure within the 23 May 2007 Perryton, Texas, supercell. *Mon. Wea. Rev.,* **139,** 3730–3749, doi:10.1175/MWR-D-10-05078.1.

——, ——, M. M. French, H. B. Bluestein, P. M. Markowski, and Y. P. Richardson, 2014: VORTEX2 observations of a low-level mesocyclone with multiple internal rear-flank downdraft momentum surges in the 18 May 2010 Dumas, Texas, supercell. *Mon. Wea. Rev.,* **142,** 2935–2960, doi:10.1175/MWR-D-13-00240.1.

Snyder, J. C., H. B. Bluestein, V. Venkatesh, and S. J. Frasier, 2013: Observations of polarimetric signatures in supercells by an X-Band mobile Doppler radar. *Mon. Wea. Rev.,* **141,** 3–29, doi:10.1175/MWR-D-12-00068.1.

Straka, J. M., E. N. Rasmussen, and S. E. Fredrickson, 1996: A mobile mesonet for finescale meteorological observations. *J. Atmos. Oceanic Technol.,* **13,** 921–936, doi:10.1175/1520-0426(1996)013<0921:AMMFFM>2.0.CO;2.

Taylor, G. I., 1938: The spectrum of turbulence. *Proc. Roy. Soc. London,* **164,** 476–490, doi:10.1098/rspa.1938.0032.

Trapp, R. J., and C. A. Doswell III, 2000: Radar data objective analysis. *J. Atmos. Oceanic Technol.,* **17,** 105–120, doi:10.1175/1520-0426(2000)017<0105:RDOA>2.0.CO;2.

Waugh, S., and S. E. Fredrickson, 2010: An improved aspirated temperature system for mobile meteorological observations, especially in severe weather. *25th Conf. on Severe Local Storms,* Denver, CO, Amer. Meteor. Soc., P5.2. [Available online at https://ams.confex.com/ams/25SLS/webprogram/Paper176205.html.]

Wicker, L. J., and R. B. Wilhelmson, 1995: Simulation and analysis of tornado development and decay within a three-dimensional supercell thunderstorm. *J. Atmos. Sci.,* **52,** 2675–2703, doi:10.1175/1520-0469(1995)052<2675:SAAOTD>2.0.CO;2.

Wurman, J., J. Straka, E. Rasmussen, M. Randall, and A. Zahrai, 1997: Design and deployment of a portable, pencil-beam, pulsed, 3-cm Doppler radar. *J. Atmos. Oceanic Technol.,* **14,** 1502–1512, doi:10.1175/1520-0426(1997)014<1502:DADOAP>2.0.CO;2.

——, D. Dowell, Y. Richardson, P. Markowski, E. Rasmussen, D. Burgess, L. Wicker, and H. Bluestein, 2012: The second Verification of the Origins of Rotation in Tornadoes Experiment: VORTEX2. *Bull. Amer. Meteor. Soc.,* **93,** 1147–1170, doi:10.1175/BAMS-D-11-00010.1.